

The properties of the quasars astrometric solution in Gaia DR2

Shilong Liao^{1,2}, Zhaoxiang Qi^{1,2}, Beatrice Bucciarelli³, Sufen Guo^{1,2}, Zihuang Cao⁴, and Zhenghong Tang^{1,2}

¹ Shanghai Astronomical Observatory, Chinese Academy of Sciences, 80 Nandan Road, Shanghai 200030, China
e-mail: shilongliao@shao.ac.cn

² School of Astronomy and Space Science, University of Chinese Academy of Sciences, Beijing 100049, China

³ INAF - Osservatorio Astrofisico di Torino, Strada Osservatorio, 2010025 Pino Torinese (TO), Italy

⁴ National Astronomical Observatory, Chinese Academy of Sciences, 20A Datun Road, Chaoyang District, Beijing, China

Received Month day, 2018; accepted Month day, 2018

ABSTRACT

Aims. The second release of Gaia Release 2 (Gaia DR2) contains the astrometric parameters for more than half a million quasars after cross matching with the prototype of the upcoming ICRF3 and the AllWISE AGN catalog. These quasars are used to define and materialize a kinematically non-rotating reference frame in optical band and to estimate the systematics in the parallaxes. We aim to evaluate the properties of the quasars astrometric solution.

Methods. Besides the quasars from the AllWISE AGN catalog, we also cross match the quasars from LQAC3, SDSS DRQ14 and LAMOST DR5 with the Gaia DR2. The final quasar sample (designated as Known Quasars Catalog for Gaia mission, KQCG) contains 779349 objects. With this quasars sample, we estimate the global bias in parallax and proper motion, analysis the proper motion field with the vector spherical harmonics (VSH) functions and compare the results with different quasars subsets. The parallaxes are expanded with the scalar spherical harmonics. The positional comparisons between the ICRF2 sources and their counterparts in Gaia DR2 are also carried out.

Results. The mean global parallaxes bias for the KQCG quasars is -0.0308 mas, and the median parallax is -0.0283 mas. For the high-precision subset ($\sigma_\omega < 1$ mas), the corresponding values are -0.0278 mas and -0.0277 mas. The VSH analysis result of KQCG shows a different rotation compared with the Gaia-CRF2 quasars sample in the proper motion field. The rotations of different samples are not larger than $10 \mu\text{as/yr}$ for each axis, with the typical glide vector of KQCG is around $(-8, +10, +9) \pm 2 \mu\text{as/yr}$. There is a $\sim +0.01$ mas/yr bias in the declination direction of the proper motion, and the typical glide of the proper motion field is $(-9, +9, 0) \pm 2 \mu\text{as/yr}$ after subtracting the bias in μ_δ . The quasars sample used to define the Gaia reference frame shows a different rotation in northern $((+2.2, +2.8, -1.5) \pm 2.0 \mu\text{as/yr})$ and southern $((+9.5, +8.7, +0.8) \pm 2.3 \mu\text{as/yr})$ hemisphere. The scalar harmonics spherical expansions of the parallaxes show a significant RMS value about $23 \mu\text{as}$ for the harmonic degree $l = 4$. No significant rotation is found between ICRF2 sources and their counterparts in Gaia DR2.

Key words. reference frame – parallax bias – proper motions – quasars

1. Introduction

The second Gaia data release (Gaia DR2) contains results for 1.693 billion sources from magnitude 3 to 21 based on the observations of the European Space Agency Gaia satellite during the period of 22 months between 2014 July 25 and 2016 May 23 (Lindgren (2018), hereafter denoted as Gaia-DR2 Astrometric paper). 1332 millions sources are provided with five astrometric parameters (positions, parallaxes, and proper motions). An additional 361 million sources, mostly faint sources, are provided with approximate positions at the reference epoch J2015.5. For the sources with five-parameter astrometric solutions, the median uncertainty in parallax and position at the reference epoch J2015.5 is about 0.04 mas for bright ($G < 14$ mag) sources, 0.1 mas at $G = 17$ mag, and 0.7 mas at $G = 20$ mag. In the proper motion components, the corresponding uncertainties are 0.05, 0.2, and 1.2 mas yr^{-1} , respectively (Lindgren (2018)).

Quasars (or QSOs) are extremely distant and small in apparent size. They are ideal objects in establishing reference frame since they present no significant parallax or proper motion. Among of the astrometric solution, Gaia DR2 provides more than 550 000 quasars, obtained from a positional cross-

match with the ICRF3-prototype and AllWISE AGN catalog, with complete five astrometric parameters - positions, parallaxes, and proper motions (Lindgren (2018)). With these half a million quasars, a kinematically non-rotating reference frame (the celestial reference frame of Gaia DR2, Gaia-CRF2) in the optical domain is defined (Mignard (2018), hereafter in denote as Gaia-CRF2 paper). The optical positions for 2843 sources in common with the unpublished ICRF3-prototype with accurate VLBI positions are used to align the axes of Gaia-CRF2 with the ICRF radio frame. From these quasars and validation solutions, the systematics in the parallaxes depending on position, magnitude, and colour are estimated with a value below 0.1 mas. Besides, there is an overall negative bias of about 0.03 mas (Lindgren (2018)).

However, besides quasars from the AllWISE AGN catalog (Secrest (2015)), there are other quasar catalogues that can enlarge the sample of quasars in Gaia DR2. To maximize the number of QSOs/AGNs, in addition to the quasars from AllWISE, we choose three samples for their huge number of reliable QSOs/AGNs. We started from the third Large Quasar Astrometric Catalogue (LQAC3) (Souhay (2015)). LQAC3 contains the QSOs/AGNs discovered in 2dF/2QZ survey (Croom (2004)), the DR10Q of the SDSS-III (Bolton (2012); Pâris (2014)) and

radio quasars listed in ICRF2, VLBA, VLA, and JVAS catalogs. And also the quasars from Hewitt & Burbidge catalog (Hewitt (1993)) and Véron-Cetty & Véron catalog (Véron (2010)). Here in this compilation, the quasars from SDSS in LQAC3 will be updated with the latest spectroscopically confirmed quasars in the SDSS-DR14 Quasar Catalog (Pâris (2017)) by using data from the Baryon Oscillation Spectroscopic Survey (BOSS; Eisenstein (2015)) and photometrically selected quasar in SDSS. And then enter the spectroscopically confirmed quasars in LAMOST DR5 (see <http://dr5.lamost.org> for more detail) using LAMOST spectroscopic data (Cui (2012)). All these quasars have been compiled into a catalog (Liao (2018)), which contains 1843850 objects.

This work aims to provide an overall analysis of the quasars astrometric solution in Gaia DR2. We begin with the global parallax and proper motion bias analysis in section 3 after the selection of the quasars in section 2. In section 4, we implement the vector spherical harmonics analysis of the selected quasars and compare the results with different quasars subsets. The scalar spherical harmonics analysis of the parallaxes is presented in section 5, with the comparison of the ICRF2 sources and their counterparts in Gaia DR2 followed in section 6. The last section is the conclusion.

2. Selection of quasars

To find the quasars in Gaia DR2, we use the following joint conditions to select quasars as adopted by the Gaia DR2 astrometric paper (Lindgren (2018)) to reduce the risk of contamination by the stars:

- (i) $\text{astrometric_matched_observations} \geq 8$,
- (ii) $\text{astrometric_params_solved}=31$,
- (iii) $|(\omega + 0.029\text{mas})/\sigma_\omega| < 5$,
- (iv) $(\mu_{\alpha^*}/\sigma_{\mu_{\alpha^*}})^2 + (\mu_\delta/\sigma_{\mu_\delta})^2 < 25$,
- (v) $|\sin b| > 0.1$
- (vi) $\rho < (2 \text{ arcsec}) \times |\sin b|$

Where ρ is the radius for the positional matching, b is the Galactic latitude. Under these conditions, 779349 quasars are found in the Gaia DR2 (denoted as KQCG in the rest of this paper). Among of them, 555934 sources are already found in the Gaia DR2 astrometric paper, which means that there are 223415 additional quasars. See the Figure 1 and 2 for the sky density distribution. The G magnitude histogram of the KQCG quasars is showed in Figure 3, most of the 223415 additional quasars are fainter than magnitude 19. The distribution of the parallaxes and the proper motions of these additional sources can be found in Figure 4 and Figure 5.

3. Global bias analysis

3.1. Parallax bias analysis

Quasars are ideal objects to check the parallax zero point since they present no significant parallax. The parallaxes for the whole KQCG quasars sample versus magnitude and colour are showed in figure 6. The mean and the median parallax of the KQCG sample is -0.0308 mas and -0.0283 mas , respectively. For the high-precision subset ($\sigma_\omega < 1 \text{ mas}$, 650232 objects), the corresponding values are -0.0278 mas and -0.0277 mas . These value agree with the results in Gaia-DR2 Astrometric paper (Lindgren (2018)). In the top panel of Figure 7, the parallax against the Ecliptic latitude does not show the roughly quadratic variation with $\sim 0.01 \text{ mas}$ smaller towards the ecliptic poles as found

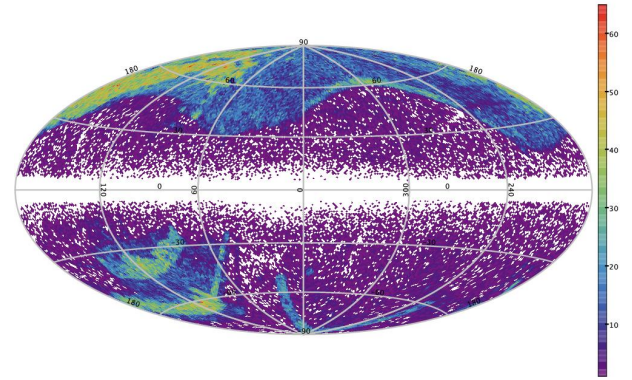


Fig. 1. The sky distribution of the 223415 additional quasars in KQCG found in Gaia DR2. The map shows the sky density with each cell of approximately 0.84 deg^2 , using the Hammer-Aitoff projection in Galactic coordinates with zero longitude at the centre and increasing longitude from right to left.

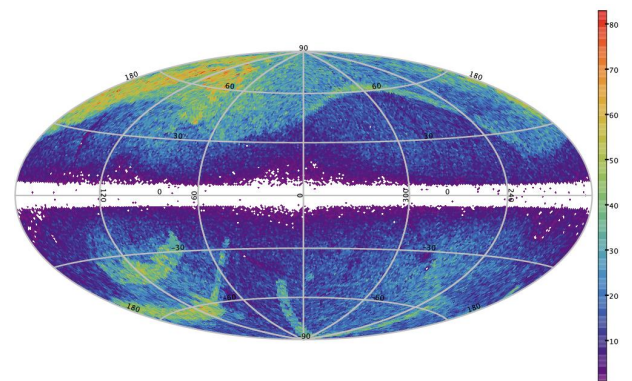


Fig. 2. The sky distribution of the total 779349 KQCG quasars found in Gaia DR2. The map shows the sky density with each cell of approximately 0.84 deg^2 , using the Hammer-Aitoff projection in Galactic coordinates with zero longitude at the centre and increasing longitude from right to left.

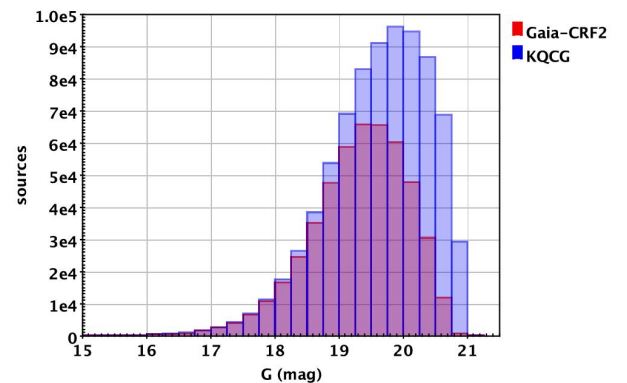


Fig. 3. G magnitude distribution of the Gaia-CRF2 sources and the KQCG sources.

in the Gaia-DR2 Astrometric paper (Lindgren (2018)). We plot the magnitude distribution of the KQCG quasars sample versus the Ecliptic latitude in the bottom panel of Figure 7, and find that the magnitude median is quiet stable ($G \sim 19.7$) along the Ecliptic latitude. We believe the quadratic variation with $\sim 0.01 \text{ mas}$ found in the Gaia-DR2 astrometric paper is caused by the sources around the Ecliptic poles are fainter in general, see Figure 9 for the magnitude sky distribution. We also plot the par-

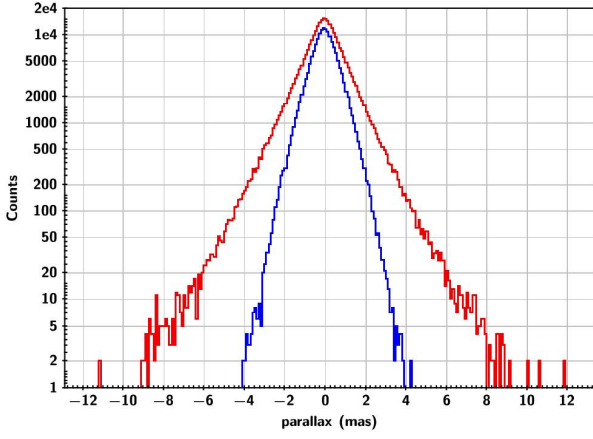


Fig. 4. Parallaxes distribution for 223415 additional quasars in KQCG. Outer (red) curve is the whole 223415 sample; Inner (blue) is the sub-sample of 166122 sources with $\sigma_\omega < 1$ mas.

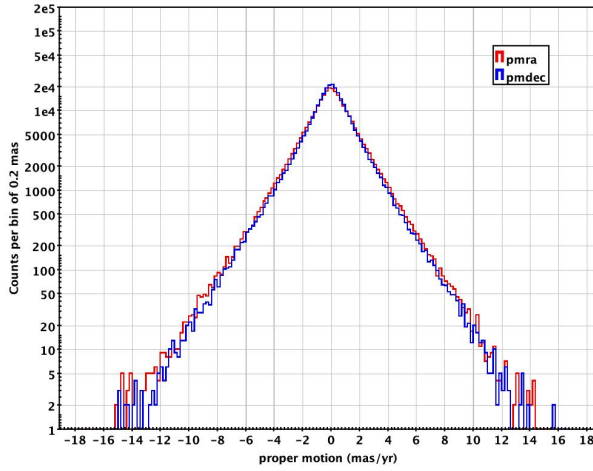


Fig. 5. Proper motions distribution for 223415 additional quasars in KQCG. The red curve is the proper motions in right ascension (pmra, μ_{α^*}) and the blue is the proper motions in declination (pmdec, μ_δ).

allax against the Galactic longitude, see Figure 8, the median magnitude varies half magnitude along the Galactic longitude. With the brighter median magnitude, the parallax bias is larger in depletion zones at $[320^\circ, 360^\circ]$ and $[0^\circ, 10^\circ]$.

3.2. Proper motion bias analysis

Quasars are extremely distant objects. Besides parallaxes, the proper motions of quasars are nominally zero for those selected for the reference frame (the Galactic acceleration effect is neglected here). In this section, we try to perform the global statistics to investigate their global quality. We plot the distribution of the proper motion versus the magnitude and the effective wavenumber of two quasars sample: KQCG and those quasars used for the Gaia-CRF2 frame rotation (they are denoted as Type2+Type3, see section 4.). The mean and median proper motion of the KQCG sample is $-1.2 \mu\text{as/yr}$ and $-2.4 \mu\text{as/yr}$ in right ascension, $+10.4 \mu\text{as/yr}$ and $+11.3 \mu\text{as/yr}$ in declination, respectively. For Type2+Type3 sample, the result is $-0.4 \mu\text{as/yr}$ and $-1.3 \mu\text{as/yr}$ in right ascension, $+12.0 \mu\text{as/yr}$ and $+11.7 \mu\text{as/yr}$ in declination. See Figure 10 and Figure 11 for the proper motion versus magnitude and colour. There is a proper motion bias of $+10 \mu\text{as/yr}$ level in declination.

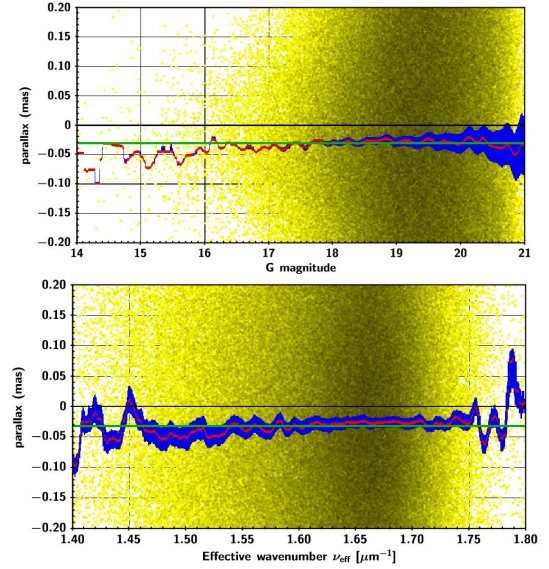


Fig. 6. Parallaxes for the all KQCG quasars plotted against Gaia G magnitude (top), colour (bottom). As adopted by the Gaia-DR2 Astrometric paper (Lindgren (2018)), only the scale between $[-0.2, 0.2]$ mas is plotted. The yellow dots are the parallax data points, the green line is the -0.0308 mas mean parallax for the full KQCG sample, while the red lines are the parallax medians ω_{med} of each running-bin, the blue curves represent the interval of $[0.98\omega_{med}, 1.02\omega_{med}]$. The same apply hereafter in.

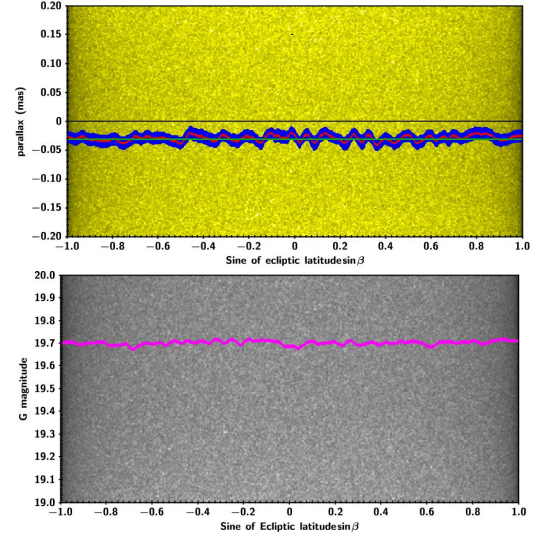


Fig. 7. Parallaxes for the KQCG quasars plotted against ecliptic latitude (top) and the Gaia G magnitude plotted against the ecliptic latitude (bottom). In the top panel, the yellow dots are the parallax data points, the black line represents the zero parallax value, the green line is the -0.0308 mas mean parallax for the full KQCG sample, while the red lines are the parallax ω_{med} medians of each running bin, the blue curves represent the interval of $[0.98\omega_{med}, 1.02\omega_{med}]$. In the bottom panel, the gray dots are the magnitude data points, only the scale $[19, 20]$ for G magnitude are plotted. The pink line is the magnitude median of the running-bin.

4. Vector spherical harmonics analysis of the proper motion field

In this section, we perform the vector spherical harmonics (VSH) analysis of different quasars samples. The proper motions spatial distribution of the KQCG quasars are shown in

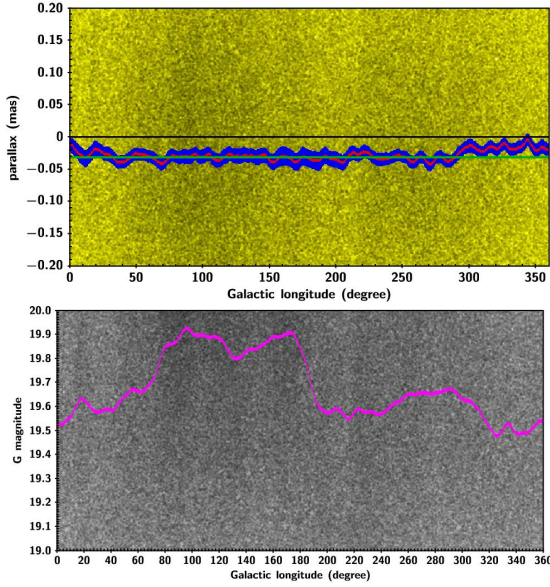


Fig. 8. Parallaxes for the KQCG quasars plotted against galactic longitude (top) and the Gaia G magnitude plotted against the Galactic longitude (bottom). In the top panel, the yellow dots are the parallax data points, the black line represents the zero parallax value, the green line is the -0.0308 mas mean parallax for the full KQCG sample, while the red lines are the parallax medians ω_{med} of each running-bin, the blue curves represent the interval of $[0.98\omega_{med}, 1.02\omega_{med}]$. In the bottom panel, the gray dots are the magnitude data points, only the scale between $[19, 20]$ for G magnitude are plotted. The pink line is the magnitude median of each running-bin.

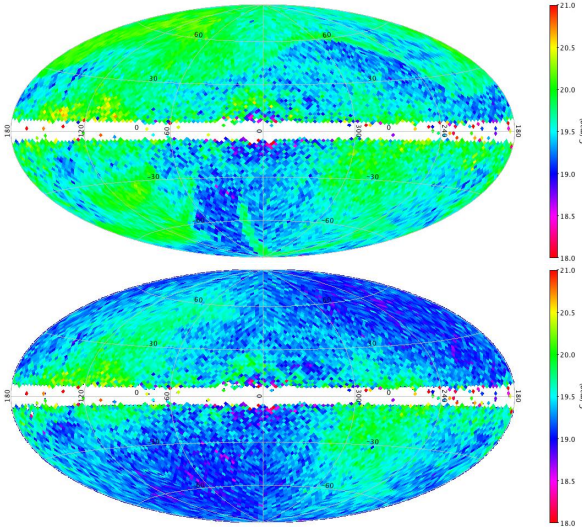


Fig. 9. Spatial distribution of the magnitude of the KQCG (top) and Gaia-CRF2 (bottom) sample in Galactic coordinates. This map is in Aitoff projection with Galactic longitude zero at the center and increasing from left to right. Median values are computed in cells of approximately 3.357deg^2 . In general, quasars of Gaia-CRF2 around the Ecliptic poles are fainter than other regions.

Figure 12. The VSH model explained by Mignard & Klioner (Mignard (2012)) is adopted. To have a better comparison of the analysis results, five groups of quasars subsets are investigated: the KQCG quasars sample (denoted as KQCG), the Gaia-CRF2 quasars sample (denoted as GCRF2), the 489163 AllWISE AGN indicated in the Gaia Archive by the field *frame_rotator_object_type* = 3 (denoted as Type3 here) used

to determine the kinematically non-rotating celestial frame, and 2843 sources matched to the ICRF3 prototype and indicated by *frame_rotator_object_type* = 2 (denoted as Type2 here) and the combination of Type2 and Type3 (denoted as Type2+Type3).

The results of the VSH analysis are listed in table 1. The rotation of the KQCG sample change from about $10\mu\text{as/yr}$ with the harmonics of degree $l = 1$ to a few $\mu\text{as/yr}$ with $l = 5$ may caused by the not uniform spatial distribution of the KQCG quasars sample. The rotation results of KQCG agree with the results of Type2+Type3 sample, although a larger value in y component. While the GCRF2 sample result shows a very different rotation, especially in x and y components. The faint end ($G \geq 19$) and the bright end ($G < 19$) of KQCG sample show a very different rotation (especially x and y component), this is consistent with the result of GCRF2 and the Type2+Type3 sample. With the much less number, the VSH analysis result of Type2 sample does not show any significant signal as the other samples. Even though the rotation results of different sample vary from each other, the rotations of them are not larger than $10\mu\text{as/yr}$ for each axis.

The glide vector of KQCG is $(-8.7 \pm 2.9, +9.6 \pm 2.3, +8.9 \pm 2.7)\mu\text{as/yr}$. This result agrees with the other sample, while the y component of the GCRF2 sample relatively smaller. As found in the 3.2, there is a global bias in μ_δ , if we subtract the bias in μ_δ (that is $\mu_\delta - \bar{\mu}_\delta$) before performing the VSH analysis, the typical glide is $(-9, 9, 0) \pm 2\mu\text{as/yr}$, where the glide in z axis can be treated as zero within the error, see the rows marked with * in table 1.

If we consider only the rotation, then we have (Mignard (2012)):

$$\begin{aligned}\mu_{\alpha*} &= -w_X \cos \alpha \sin \delta - w_Y \sin \alpha \sin \delta + w_Z \cos \delta \\ \mu_\delta &= +w_X \sin \alpha - w_Y \cos \alpha\end{aligned}\quad (1)$$

Where w_X , w_Y , and w_Z are the three rotation rate of the proper motion field. We use this equation to further investigate the sources of KQCG and Type2+Type3 in Northern and Southern hemisphere, respectively. The results are shown in table 2. For the Type2 quasars, no significant rotation is found. For Type2+Type3 quasars, the x and y components of the rotation in southern hemisphere are more significant than the northern hemisphere. For KQCG sample, the rotation of x and y component agrees with each other in northern and southern hemisphere, while the z component is more significant in northern hemisphere.

If we try to estimate the proper motion bias in μ_δ (denoted as $d\mu_\delta$ here), an additional term should be added in Equation (1):

$$\begin{aligned}\mu_{\alpha*} &= -w_X \cos \alpha \sin \delta - w_Y \sin \alpha \sin \delta + w_Z \cos \delta \\ \mu_\delta &= +w_X \sin \alpha - w_Y \cos \alpha + d\mu_\delta\end{aligned}\quad (2)$$

The results can be found in table 2. The estimated bias in μ_δ is consistent within error between these two quasars samples.

5. The scalar field of parallaxes

The parallaxes of the quasars can be treated as parallax residuals. Parallaxes can be seen as the radial part of the spatial positions differences on the celestial sphere, see Figure 13 for the parallax sky distribution of KQCG sample. Here in this section, we try to analysis the parallax residuals using the scalar spherical harmonics as follows (Bucciarelli (2011)):

$$V_\pi(\alpha, \delta) = \Delta\pi = \sum_l \sum_{m=-l}^l c_{lm} Y_{lm}(\alpha, \delta) \quad (3)$$

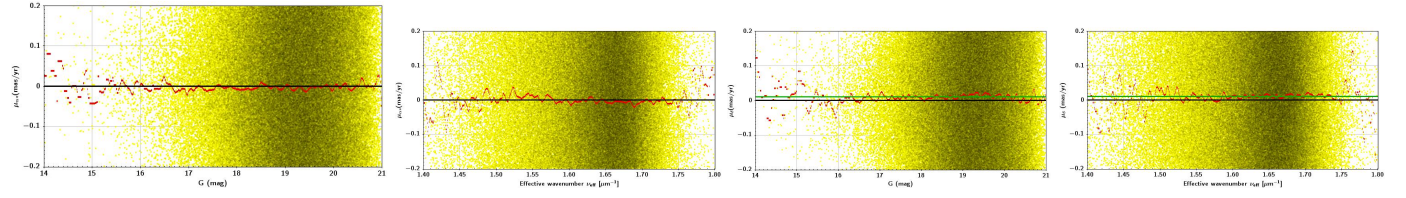


Fig. 10. Proper motions for the all KQCG quasars plotted against the Gaia G magnitude and colour (The first and second figure from the left is for μ_{α^*} , and the third and fourth is for μ_{δ}). The yellow dots are the proper motion data. The black line represents the zero value, the green lines in the two figures on the right is the $+10.4 \mu\text{as/yr}$ mean μ_{δ} , while the red lines are the proper motion medians μ_{med} of each running-bin.

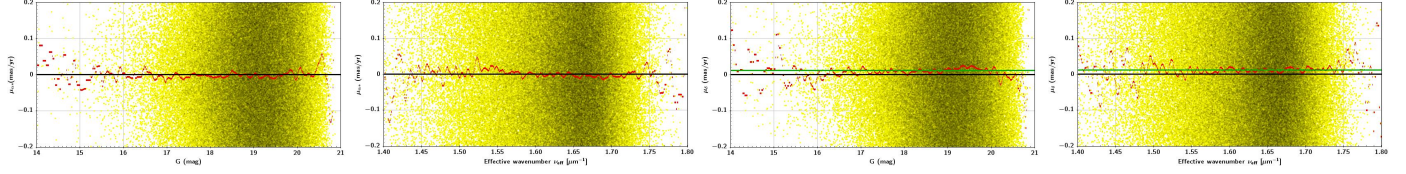


Fig. 11. Proper motions for the all Type2+Type3 quasars plotted against the Gaia G magnitude and colour (The first and second figure from the left is for μ_{α^*} , and the third and fourth is for μ_{δ}). The yellow dots are the proper motion data. The black line represents the zero value, the green lines in the two figures on the right is the $+12.0 \mu\text{as/yr}$ mean μ_{δ} , while the red lines are the proper motion medians μ_{med} of each running-bin.

Table 1. VSH analysis of the proper motion field of different quasars samples in Gaia DR2. The VSH analysis results of GCRF2 sample (the last four rows) are taken from the Table 2 of the Gaia-CRF2 paper (Mignard (2018)). The number of Type 3 sample is less than 489163 is because there are 3178 of them do not contain the parallax solution. The row * means the bias in μ_{δ} is subtracted (that is $\mu_{\delta} = \mu_{\delta} - \mu_{\delta}$) when perform the VSH analysis.

| Source Subset | l_{max} | N | Rotation [$\mu\text{as/yr}$] | | | Glide [$\mu\text{as/yr}$] | | |
|----------------------------------|------------------|--------|--------------------------------|-----------------|-----------------|-----------------------------|-----------------|-----------------|
| | | | x | y | z | x | y | z |
| KQCG | 1 | 779349 | 12.8 \pm 2.0 | 11.5 \pm 1.7 | -3.9 \pm 2.1 | -7.3 \pm 2.1 | 10.2 \pm 1.9 | 12.0 \pm 2.1 |
| | 5 | 779349 | 1.9 \pm 2.6 | 6.5 \pm 2.2 | 6.7 \pm 2.7 | -8.7 \pm 2.9 | 9.6 \pm 2.3 | 8.9 \pm 2.7 |
| | * | 779349 | 1.9 \pm 2.6 | 6.5 \pm 2.2 | 6.7 \pm 2.7 | -8.6 \pm 2.9 | 9.6 \pm 2.3 | -3.3 \pm 2.7 |
| $G \geq 19$ | 1 | 615496 | 16.2 \pm 2.5 | 15.7 \pm 2.2 | -4.5 \pm 2.6 | -7.6 \pm 2.7 | 10.9 \pm 2.4 | 10.1 \pm 2.6 |
| | 5 | 615496 | 3.5 \pm 3.4 | 11.2 \pm 2.8 | 7.8 \pm 3.5 | -8.4 \pm 3.8 | 10.0 \pm 2.9 | 6.5 \pm 3.5 |
| $G < 19$ | 1 | 163853 | 1.1 \pm 1.5 | -3.7 \pm 1.3 | -2.3 \pm 1.5 | -9.5 \pm 1.6 | 9.4 \pm 1.4 | 18.1 \pm 1.5 |
| | 5 | 163853 | -2.3 \pm 2.0 | -8.6 \pm 1.7 | 2.4 \pm 1.9 | -11.8 \pm 2.2 | 8.0 \pm 1.7 | 15.3 \pm 1.9 |
| Type2+Type3 | 1 | 488828 | 5.4 \pm 1.6 | 5.0 \pm 1.5 | -0.2 \pm 1.8 | -9.2 \pm 1.7 | 6.6 \pm 1.6 | 16.4 \pm 1.8 |
| | 5 | 488828 | 2.0 \pm 1.9 | 1.9 \pm 1.7 | 6.3 \pm 2.1 | -9.2 \pm 2.2 | 8.5 \pm 1.8 | 13.7 \pm 2.1 |
| | * | 488828 | 2.0 \pm 2.0 | 1.9 \pm 1.7 | 6.4 \pm 2.1 | -9.1 \pm 2.2 | 8.5 \pm 1.8 | -0.4 \pm 2.1 |
| $G \geq 19$ | 1 | 363558 | 7.2 \pm 2.0 | 8.3 \pm 1.9 | -0.5 \pm 2.3 | -8.8 \pm 2.1 | 5.5 \pm 2.1 | 16.2 \pm 2.3 |
| | 5 | 363558 | 3.5 \pm 2.5 | 6.6 \pm 2.2 | 5.5 \pm 2.7 | -8.8 \pm 2.8 | 8.0 \pm 2.3 | 14.2 \pm 2.7 |
| $G < 19$ | 1 | 125270 | 0.3 \pm 1.7 | -4.2 \pm 1.5 | -0.1 \pm 1.8 | -11.0 \pm 1.9 | 9.7 \pm 1.7 | 17.7 \pm 1.8 |
| | 5 | 125270 | -0.1 \pm 2.3 | -8.3 \pm 1.9 | 5.6 \pm 2.4 | -10.9 \pm 2.6 | 10.2 \pm 2.1 | 14.3 \pm 2.4 |
| Type3 | 1 | 485985 | 5.4 \pm 1.6 | 4.8 \pm 1.5 | -0.3 \pm 1.8 | -9.1 \pm 1.7 | 6.6 \pm 1.6 | 16.3 \pm 1.8 |
| | 5 | 485985 | 2.0 \pm 1.9 | 1.6 \pm 1.7 | 6.4 \pm 2.1 | -9.2 \pm 2.2 | 8.6 \pm 1.8 | 13.6 \pm 2.1 |
| Type2 | 1 | 2843 | -5.7 \pm 20.9 | 27.5 \pm 19.6 | 14.2 \pm 40.5 | -10.5 \pm 30.6 | 1.5 \pm 30.1 | 32.2 \pm 40.5 |
| | 5 | 2843 | 28.6 \pm 29.2 | 36.0 \pm 29.3 | 13.7 \pm 43.2 | -10.5 \pm 41.2 | 20.0 \pm 38.1 | 30.0 \pm 43.2 |
| GCRF2 | 1 | 556869 | -3.6 \pm 0.8 | -2.2 \pm 0.7 | -0.9 \pm 0.9 | -7.0 \pm 0.8 | 4.7 \pm 0.7 | 12.1 \pm 0.7 |
| | 5 | 556869 | -5.5 \pm 1.1 | -7.4 \pm 0.9 | 5.6 \pm 1.2 | -9.2 \pm 1.2 | 4.7 \pm 1.0 | 11.6 \pm 1.0 |
| $G > 19$ | 5 | 406356 | 9.8 \pm 2.1 | 6.2 \pm 1.8 | 7.0 \pm 2.4 | -8.3 \pm 2.3 | 3.3 \pm 1.9 | 15.6 \pm 1.9 |
| $G < 19, \mu < 2 \text{ mas/yr}$ | 5 | 149146 | -11.2 \pm 1.3 | -12.0 \pm 1.1 | 4.4 \pm 1.4 | -9.8 \pm 1.5 | 4.6 \pm 1.2 | 10.4 \pm 1.1 |

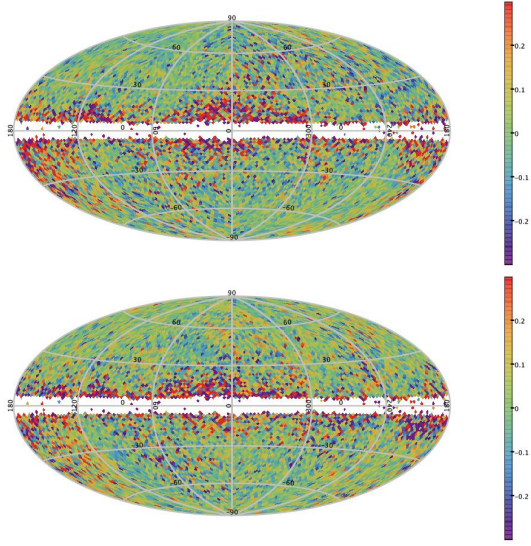


Fig. 12. Spatial distribution of the proper motions of the KQCG sample in Galactic coordinates. This map is in Aitoff projection with Galactic longitude zero at the center and increasing from left to right. Median values are computed in cells of approximately 3.357deg^2 .

Table 2. Global rotation rate from the KQCG, Type2 and Type3 quasars. "-" means no estimation.

| Subset | w_X ($\mu\text{as/yr}$) | w_Y ($\mu\text{as/yr}$) | w_Z ($\mu\text{as/yr}$) | $d\mu_\delta$ ($\mu\text{as/yr}$) |
|-------------|--------------------------------|--------------------------------|--------------------------------|--|
| Type2 | -4 ± 20 | 28 ± 19 | 14 ± 40 | - |
| North | 0 ± 29 | 21 ± 27 | 30 ± 35 | - |
| South | 4 ± 32 | 35 ± 30 | -4 ± 60 | - |
| Type2+Type3 | 5.8 ± 1.6 | 5.3 ± 1.5 | -0.3 ± 1.8 | - |
| | 5.3 ± 1.6 | 4.8 ± 1.5 | -0.2 ± 1.8 | 11.7 ± 1.2 |
| North | 2.2 ± 2.2 | 2.8 ± 2.0 | -1.5 ± 2.5 | - |
| | 5.2 ± 2.2 | -1.5 ± 2.1 | -1.5 ± 2.5 | 15.2 ± 4.0 |
| South | 9.5 ± 2.3 | 8.7 ± 2.2 | 0.8 ± 2.3 | - |
| | 7.0 ± 2.4 | 10.7 ± 2.2 | 0.8 ± 2.3 | 10.1 ± 1.9 |
| KQCG | 11.5 ± 1.9 | 11.4 ± 1.7 | -4.4 ± 2.1 | - |
| | 11.0 ± 2.0 | 10.1 ± 1.7 | -4.3 ± 2.1 | 9.2 ± 1.4 |
| North | 8.1 ± 2.6 | 10.5 ± 2.2 | -8.0 ± 2.8 | - |
| | 9.2 ± 2.6 | 6.3 ± 2.4 | -8.1 ± 2.8 | 10.9 ± 2.0 |
| South | 15.8 ± 3.1 | 13.4 ± 2.7 | 1.3 ± 2.8 | - |
| | 13.7 ± 3.1 | 15.4 ± 2.8 | 1.3 ± 2.8 | 8.6 ± 2.5 |

Where Y_{lm} are the standard spherical functions defined here the following sign convention:

$$Y_{lm} = (-1)^m \sqrt{\frac{2l+1}{4\pi} \frac{(l-m)!}{(l+m)!}} P_{lm}(\sin \delta) e^{im\alpha} \quad (4)$$

for $m \geq 0$ and we have $Y_{l,-m}(\alpha, \delta) = (-1)^m Y_{lm}^*(\alpha, \delta)$ for $m < 0$. The * denotes complex conjugation. $P_{lm}(x)$ is the associated Legendre functions.

The equation 3 can be reduced as:

$$\Delta\pi = \sum_{l=1}^{l_{\max}} \left[c_{l0}^R Y_{l0}^R + 2 \sum_{m=1}^l (c_{lm}^R Y_{lm}^R - c_{lm}^I Y_{lm}^I) \right] \quad (5)$$

Where R and I denote the real and imaginary part of the function. The power of the expansion of different degree l is defined as

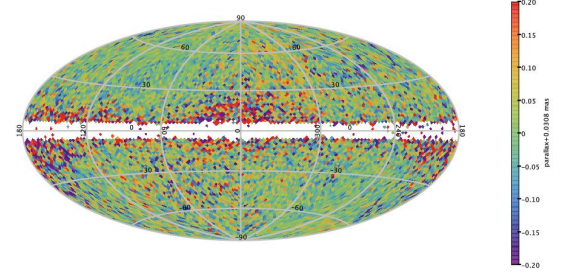


Fig. 13. Spatial distribution of the parallaxes of the KQCG sample in Galactic coordinates. This map is in Aitoff projection with Galactic longitude zero at the center and increasing from left to right. Median values are computed in cells of approximately 3.357deg^2 .

Table 3. The scalar spherical harmonics expansion of the parallaxes of the quasars sample.

| l | Type2+Type3 | | KQCG | |
|-----|---------------------------|--------------|---------------------------|--------------|
| | $P_l^{1/2}(\mu\text{as})$ | Z_{χ^2} | $P_l^{1/2}(\mu\text{as})$ | Z_{χ^2} |
| 1 | 17.5 | 6.06 | 15.7 | 5.57 |
| 2 | 10.8 | 3.22 | 12.3 | 4.09 |
| 3 | 16.3 | 5.09 | 15.9 | 5.12 |
| 4 | 23.8 | 7.98 | 21.8 | 7.48 |
| 5 | 14.7 | 4.01 | 15.3 | 4.54 |
| 6 | 12.2 | 2.41 | 11.2 | 2.05 |
| 7 | 14.1 | 3.63 | 14.7 | 4.23 |
| 8 | 10.9 | 1.44 | 10.6 | 1.47 |
| 9 | 11.6 | 2.60 | 10.4 | 2.12 |
| 10 | 12.8 | 3.12 | 13.1 | 3.71 |

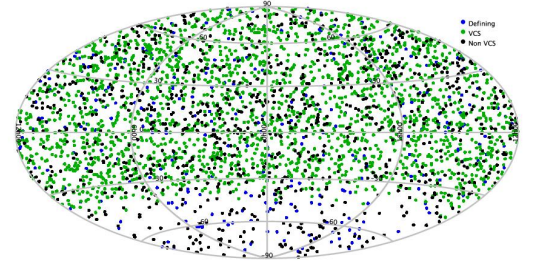


Fig. 14. ICRF2 sources sky distribution, Hammer-Aitoff projection in Equatorial coordinates. The blue dots are the 295 defining sources, while the green dots are the 2197 Very long baseline array calibrator survey (VCS) sources, and the 922 black are the non VCS sources. All defining sources are also non-VCS sources.

follows:

$$P_l = (c_{l0}^R)^2 + 2 \sum_{m=1}^l [(c_{lm}^R)^2 + (c_{lm}^I)^2] \quad (6)$$

The significant of a harmonic degree l is calculated by the equation (83) and (84) from the Mignard & Klioner (2012) paper. The analysis results of the parallaxes in the Type2+Type3 sample and the KQCG sample can be found in table 3. Both two samples show a significant harmonic level of degree 4 ($P_{l=4}^{1/2} \sim 23 \mu\text{as}$), which corresponds to an angular scale $\sim 180^\circ/l=45^\circ$.

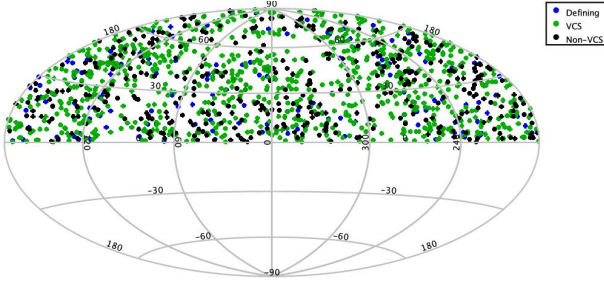


Fig. 15. Sky distribution of ICRF2 sources counterparts found in Gaia DR2, Hammer-Aitoff projection in Equatorial coordinates. The blue dots are the defining sources, while the green dots are the Very long baseline array calibrator survey (VCS) sources, and the blacks are the non VCS sources.

6. Comparison of the optical and the radio positions of ICRF2 sources

In the Gaia-CRF2 paper (Mignard (2018)), the unpublished ICRF3-prototype with accurate VLBI positions are used to align the axes of Gaia-CRF2 with the ICRF radio frame. In this section, we try to compare the angular differences the ICRF2 sources and their counterparts in Gaia DR2. The ICRF2 catalog was computed using nearly 30 years of VLBI observations and provides accurate positions of 295 “defining” sources and generally less accurate positions of 3119 other radio sources, leading to 3414 sources in total (Fey (2015)), see Figure 14 for the sky distribution.

6.1. Identification of ICRF2 sources in Gaia DR2

To find the counterparts of the ICRF2 sources in Gaia DR2 astrometric solutions, we use the following joint conditions as adopted by the Gaia-DR2 Astrometric paper:

- (i) $\rho \leq 100\text{mas}$,
- (ii) $\text{astrometric_matched_observations} \geq 8$,
- (iii) $\sigma_\omega < 1\text{ mas}$,
- (iv) $|\omega/\sigma_\omega| < 5$,
- (v) $(\mu_{\alpha^*}/\sigma_{\mu_{\alpha^*}})^2 + (\mu_{\delta^*}/\sigma_{\mu_{\delta^*}})^2 < 25$.

Where ρ is the radius for the positional matching. Under these conditions, 1321 ICRF2 sources are found in the Gaia DR2 sources see Figure 15 for the sky density. One can see that all the matched ICRF2 sources are in the northern hemisphere. The most likely explanation might be that the position errors of the sources in southern hemisphere are generally substantially worse due to small number of observation stations in the southern hemisphere (Malkin (2015)).

The angular distance between two objects is computed as:

$$\rho = (\Delta\alpha_*^2 + \Delta\delta^2)^{1/2} \quad (7)$$

Where $\Delta\alpha_* = \Delta\alpha \cos \delta$. Figure 16 gives the histogram of the angular differences. Among the matched sources, most of the angular differences are smaller than 1 mas, and also a few sources with ρ larger than 10 mas.

Figure 17 shows the angular differences ρ between the ICRF2 sources and their counterparts in Gaia DR2 with respect to the formal positional uncertainties $\sigma_{pos,max}$ of the ICRF2 sources and the Gaia DR2 sources. Most of the sources in Gaia DR2 have position uncertainties under 1 mas, while the uncertainties of the sources in ICRF2 range from 0.04mas to 10 mas with even a few of them up to tens of mas. Some sources

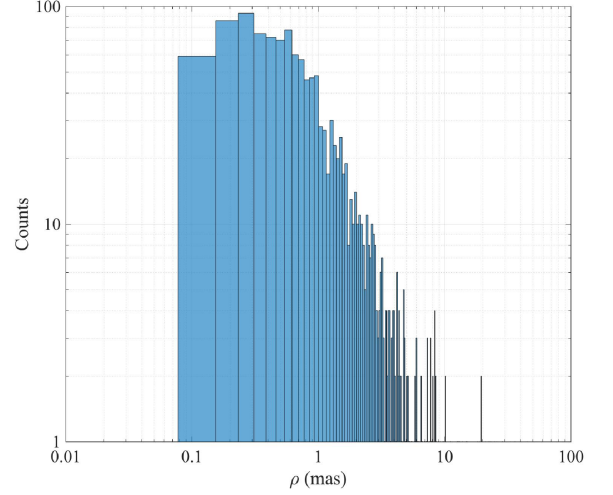


Fig. 16. Histogram of the angular differences ρ between Gaia DR2 and ICRF2 sources for 1321 common sources. The axis is log-log scale, and the bins in ρ is 0.07735 mas.

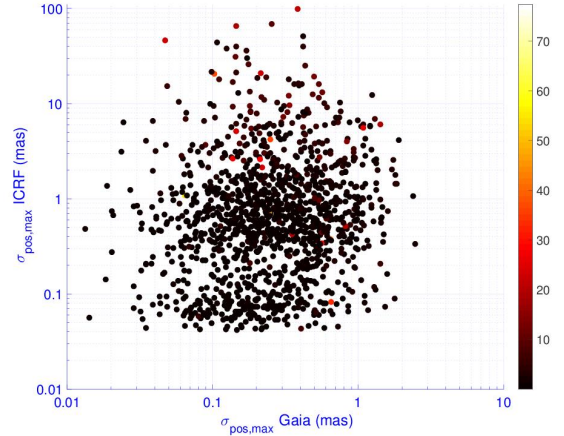


Fig. 17. The formal position uncertainties $\sigma_{pos,max}$ of the Gaia DR2 sources (abscissa) with respect to the ICRF2 sources (ordinate). The color bar on the right is the position differences ρ (in mas) between Gaia DR2 and the ICRF2 sources. The axis is log-log scale.

with small position uncertainties show large angular differences, which also happens in the Gaia DR2 sources when compared with the ICRF3 prototype (Mignard (2018)).

6.2. Systematics analysis

The alignment of the optical positions in Gaia DR2 with respect to the ICRF2 can be modelled by an infinitesimal solid rotation with the following equations (Lindgren (2016)):

$$\begin{aligned} \Delta\alpha_* &= -\epsilon_X \cos \alpha \sin \delta - \epsilon_Y \sin \alpha \sin \delta + \epsilon_Z \cos \delta \\ \Delta\delta &= +\epsilon_X \sin \alpha - \epsilon_Y \cos \alpha \end{aligned} \quad (8)$$

Where $\Delta\alpha_* = \Delta\alpha \cos \delta$. ϵ_X , ϵ_Y and ϵ_Z are the three rotation angles around the ICRS parameters.

The weighted least-squares estimation of the orientation parameters between Gaia-CRF2 and ICRF2 are listed in table 4. No significant rotation is found at the level of 0.1 mas.

Table 4. Global difference between the Gaia-CRF2 positions of ICRF sources and their positions in ICRF2.

| Source subset | N | ϵ_x (μ as) | ϵ_y (μ as) | ϵ_z (μ as) |
|---------------|------|--------------------------|--------------------------|--------------------------|
| All | 1321 | 115 ± 108 | 46 ± 105 | -56 ± 195 |
| Defining | 139 | 184 ± 72 | -58 ± 72 | -13 ± 132 |
| Non-defining | 1182 | 82 ± 124 | -14 ± 120 | -45 ± 133 |

7. Conclusions

We analysis the properties of the quasars astrometric solutions of 779349 quasars (indicated as KQCG), which is about 40% more than the Gaia-CRF2 quasars sample, the conclusions are as follows:

1. The mean global parallaxes bias for the KQCG quasars sample is -0.0308 mas and the median value is -0.0283 mas, which agrees with the results in the Gaia DR2 paper. The roughly quadratic variation with ~ 0.010 mas smaller parallaxes towards the ecliptic poles is most likely caused by the fainter sources around the ecliptic poles.
2. The VSH method is applied to the proper motion vector field of different quasars sample. The rotation result of KQCG agrees with the result of Type2+Type3 quasars sample. The GCRF2 quasars sample result shows a very different rotation with respect to KQCG. The rotations of them are not larger than $10 \mu\text{as/yr}$ for each axis. The glide vector of KQCG is $(-8.7 \pm 2.9, +9.6 \pm 2.3, +8.9 \pm 2.7) \mu\text{as/yr}$. The Type2+Type3 sample shows a different rotation in northern and southern hemisphere. While the rotation of the KQCG sample agrees in northern and southern hemisphere in x and y components.
3. There is a $\sim +0.01$ mas/yr bias in the declination direction of proper motion, and the typical glide of the proper motion field is $(-9, 8, 0) \pm 2 \mu\text{as/yr}$ after subtracting the bias in μ_δ . The expected signature for the Galactocentric acceleration is $(-0.25, -3.93, -2.18) \mu\text{as/yr}$ in the ICRS component. Clearly the bias in μ_δ is larger than the Galactocentric acceleration.
4. The scalar harmonics sphere expansion of the parallaxes show a significant harmonic degree at $l=4$ with significance of $Z_{\chi^2} > 7$.
5. The ICRF2 sources are cross matched with the Gaia DR2 sources. Only the sources in the northern hemisphere are found, which may be caused by the generally substantially worse position errors in southern hemisphere. The systematic between the ICRF2 sources and the corresponding Gaia DR2 sources is analyzed, no significant rotation signal is found.

Acknowledgements. This work has made used of data from ESA space mission Gaia, processed by the Gaia Data Processing and Analysis Consortium (DPAC). We are grateful to the developers of the TOPCAT (Taylor (2005)) software. Guoshoujing Telescope (the Large Sky Area Multi-Object Fiber Spectroscopic Telescope LAMOST) is a National Major Scientific Project built by the Chinese Academy of Sciences. Funding for the project has been provided by the National Development and Reform Commission. LAMOST is operated and managed by the National Astronomical Observatories, Chinese Academy of Sciences. This work has been supported by the grants from the National Science Foundation of China (NSFC) through grants 11703065 and 11573054.

References

- Bolton A S, Schlegel D J, Aubourg É, et al. Spectral classification and redshift measurement for the SDSS-III baryon oscillation spectroscopic survey[J]. The Astronomical Journal, 2012, 144(5): 144.
- Bucciarelli B, Abbas U, Vecchiato A, et al. Comparison of two Gaia sphere solutions using orthonormal bases on the sphere
- Croom S M, Smith R J, Boyle B J, et al. The 2dF QSO Redshift Survey–XII. The spectroscopic catalogue and luminosity function[J]. Monthly Notices of the Royal Astronomical Society, 2004, 349(4): 1397-1418.
- Cui, X. Q., Zhao, Y. H., Chu, Y. Q., et al. 2012, Research in Astronomy and Astrophysics, 12, 1197
- Eisenstein D. The Baryon Oscillation Spectroscopic Survey (BOSS): Dark Energy from the World’s Largest Redshift Survey[C]//APS April Meeting Abstracts. 2015.
- Fey A L, Gordon D, Jacobs C S, et al. The second realization of the international celestial reference frame by very long baseline interferometry[J]. The Astronomical Journal, 2015, 150(2): 58.
- Hewitt A, Burbidge G. A revised and updated catalog of quasi-stellar objects[J]. The Astrophysical Journal Supplement Series, 1993, 87: 451-947.
- Liao S., Qi Z., et al. A compilation of known QSOs for the Gaia mission[J]. arXiv preprint arXiv:1804.08821, 2018.
- Lindgren L, Lammers U, Bastian U, et al. Gaia Data Release 1: Astrometry - one billion positions, two million proper motions and parallaxes[J]. Astronomy & Astrophysics, 2016, 595.
- Lindgren L, Hernandez J, Bombrun A, et al. Gaia Data Release 2: The astrometric solution[J]. arXiv preprint arXiv:1804.09366, 2018.
- Malkin Z, Jacobs C S, Arias F, et al. The ICRF-3: Status, plans, and progress on the next generation International Celestial Reference Frame[J]. arXiv preprint arXiv:1511.08035, 2015.
- Mignard F, Klioner S. Analysis of astrometric catalogues with vector spherical harmonics[J]. Astronomy and Astrophysics, 2012, 547: A59.
- Mignard F, Klioner S, Lindgren L, et al. Gaia Data Release 2: The Celestial reference frame (Gaia-CRF2)[J]. arXiv preprint arXiv:1804.09377, 2018.
- Pâris I, Petitjean P, Aubourg É, et al. The Sloan Digital Sky Survey quasar catalogue: tenth data release[J]. Astronomy & Astrophysics, 2014, 563: A54.
- Pâris I, Petitjean P, Aubourg E, et al. The Sloan Digital Sky Survey Quasar Catalog: Fourteenth Data Release[J]. arXiv preprint arXiv:1712.05029, 2017.
- Secrest N J, Dudik R P, Dorland B N, et al. Identification of 1.4 Million Active Galactic Nuclei in the Mid-Infrared using WISE Data[J]. The Astrophysical Journal Supplement Series, 2015, 221(1): 12.
- Souchay, J., Andrei, A. H., Barache, C., et al. 2015, Astronomy and Astrophysics, 583
- Taylor M B, Shopbell P, Britton M, et al. ASP Conf. Ser. Vol. 347, Astronomical Data Analysis Software and Systems XIV[J]. 2005.
- Véron-Cetty M P, Véron P. A catalogue of quasars and active nuclei[J]. Astronomy & Astrophysics, 2010, 518: A10.